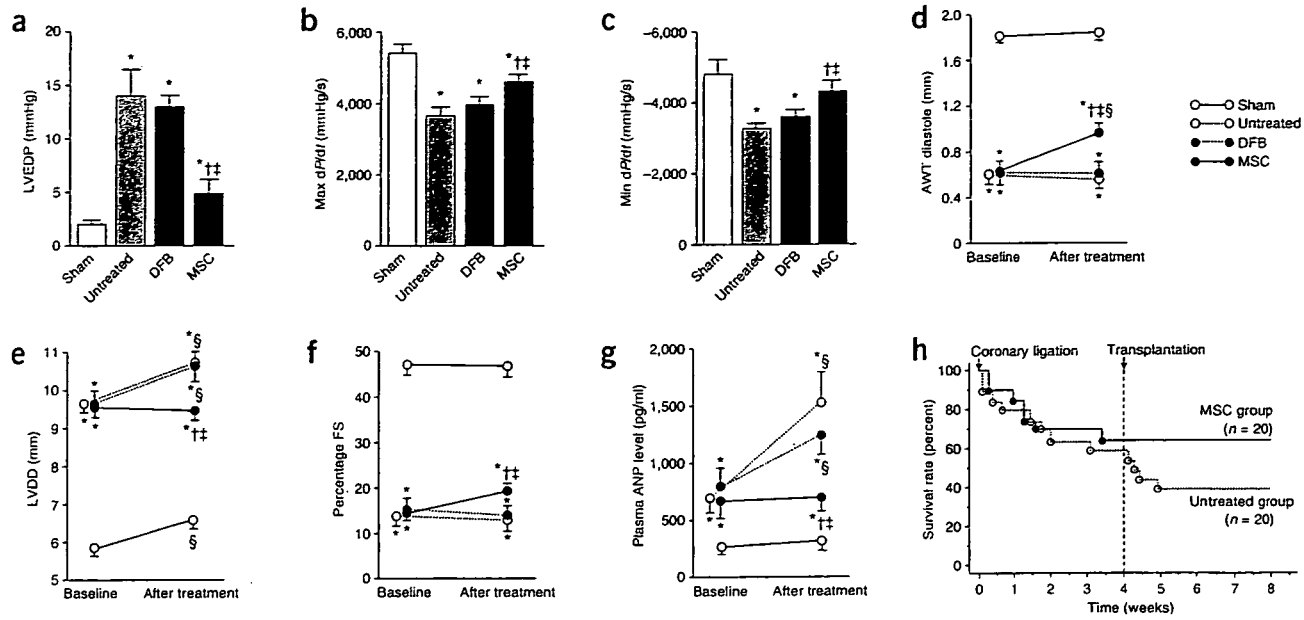

Figure 5 Cardiac structure and function after transplantation of monolayered MSCs. (**a–c**) Hemodynamic parameters obtained by catheterization. LVEDP, left ventricle end-diastolic pressure. (**d–f**) Echocardiographic findings. AWT, anterior wall thickness; LVDD, left ventricle end-diastolic dimension; FS, fractional shortening. (**g**) Plasma atrial natriuretic peptide (ANP) level. Baseline represents measurements 4 weeks after coronary ligation; 'after treatment' represents measurements taken 4 weeks after transplantation (8 weeks after coronary ligation). Data are mean ± s.e.m. $^{*}P < 0.05$ versus sham group; $^{\dagger}P < 0.05$ versus untreated group; $^{\ddagger}P < 0.05$ versus DFB group; $^{\S}P < 0.05$ versus baseline. (**h**) Survival of rats with chronic heart failure with or without monolayered MSC transplantation. The Kaplan-Meier survival curve demonstrates an 8-week survival rate of 65% for the MSC group versus 45% for the untreated group. Survival rate after transplantation was significantly higher in the MSC group than in the untreated group (100% versus 71% 4-week survival rate after transplantation, log-rank test, $P < 0.05$).

conditions at 37 °C and becomes reversibly hydrophilic below 32 °C. Therefore, cultured cells that adhere to the dish surface spontaneously detach from the grafted surface without enzymatic digestion.

Preparation of monolayered cell grafts. We suspended MSCs at the third or fourth passage from adipose tissue or DFBs at the second passage by trypsinization, and plated the cell suspension containing 3 ml of complete medium onto a 60-mm temperature-responsive dish at 5×10^5 cells per dish (MSCs) or 8×10^5 cells per dish (DFBs) and cultured cells at 37 °C. After 3 d of culture, confluently cultured MSCs or DFBs on the temperature-responsive dishes were incubated at 20 °C. By 40 min, both MSCs and DFBs detached spontaneously and floated up into the medium as monolayered cell grafts. Immediately after detachment, we gently aspirated the monolayered cell grafts using a 1,000 µl pipette tip and transferred them onto an elastic plastic sheet.

Statistical analysis. Numerical values are expressed as mean ± s.e.m. There are four groups of continuous variables in this study. Therefore, for multiple comparisons of more than two groups, we performed one-way analysis of variance (ANOVA). If the ANOVA was significant, we used the Newman-Keul procedure as a *post hoc* test. For repeated measurement such as echocardiographic parameters, we performed two-way repeated ANOVA with the Newman-Keul test. Comparisons of parameters between two groups were made by unpaired Student *t*-test. A value of $P < 0.05$ was considered significant.

Note: Supplementary information is available on the Nature Medicine website.

ACKNOWLEDGMENTS

We thank J.I. Hoffman for his statistical advice. We thank T. Iwase, T. Ito, S. Murakami, N. Sakata and Y. Isono for their technical support. We thank Y. Tsuboi and H. Sonoda for their assistance with microscopic analysis of monolayered cell grafts. We also thank Y. Sawa for his suggestions on this study. This work was supported by research grants for Cardiovascular Disease (16C-6) and Human Genome Tissue Engineering 005 and 009 from the Japanese Ministry of Health, Labor and Welfare, and the Program for Promotion of Fundamental Studies in Health Science of the Japanese National Institute of Biomedical Innovation.

COMPETING INTERESTS STATEMENT

The authors declare competing financial interests (see the *Nature Medicine* website for details).

Published online at http://www.nature.com/naturemedicine/
Reprints and permissions information is available online at http://npg.nature.com/reprintsandpermissions/

1. Liu, J. *et al.* Autologous stem cell transplantation for myocardial repair. *Am. J. Physiol. Heart Circ. Physiol.* **287**, H501–H511 (2004).
2. Reinlib, L. & Field, L. Cell transplantation as future therapy for cardiovascular disease?: A workshop of the National Heart, Lung, and Blood Institute. *Circulation* **101**, E182–E187 (2000).
3. Schuster, M.D. *et al.* Myocardial neovascularization by bone marrow angioblasts results in cardiomyocyte regeneration. *Am. J. Physiol. Heart Circ. Physiol.* **287**, H525–H532 (2004).
4. Kocher, A.A. *et al.* Neovascularization of ischemic myocardium by human bone-marrow-derived angioblasts prevents cardiomyocyte apoptosis, reduces remodeling and improves cardiac function. *Nat. Med.* **7**, 430–436 (2001).
5. Bel, A. *et al.* Transplantation of autologous fresh bone marrow into infarcted myocardium: a word of caution. *Circulation* **108**, II247–II252 (2003).
6. Yamada, N. *et al.* Thermo-responsive polymeric surface: control of attachment and detachment of cultured cells. *Makromol. Chem. Rapid Commun.* **11**, 571–576 (1990).
7. Okano, T., Yamada, H., Sakai, H. & Sakurai, Y. A novel recovery system for cultured cells using plasma-treated polystyrene dishes grafted with poly (N-isopropylacrylamide). *J. Biomed. Mater. Res.* **27**, 1243–1251 (1993).
8. Shimizu, T. *et al.* Fabrication of pulsatile cardiac tissue grafts using a novel 3-dimensional cell sheet manipulation technique and temperature-responsive cell culture surfaces. *Circ. Res.* **90**, e40–e48 (2002).
9. Hirose, M., Kwon, O.H., Yamato, M., Kikuchi, A. & Okano, T. Creation of designed shape cell sheets that are noninvasively harvested and moved onto another surface. *Biomacromolecules* **1**, 377–381 (2000).
10. Kushida, A. *et al.* Decrease in culture temperature releases monolayer endothelial cell sheets together with deposited fibronectin matrix from temperature-responsive culture surfaces. *J. Biomed. Mater. Res.* **45**, 355–362 (1999).
11. Herreros, J. *et al.* Autologous intramyocardial injection of cultured skeletal muscle-derived stem cells in patients with non-acute myocardial infarction. *Eur. Heart J.* **24**, 2012–2020 (2003).

12. Skobel, E. *et al.* Transplantation of fetal cardiomyocytes into infarcted rat hearts results in long-term functional improvement. *Tissue Eng.* **10**, 849–864 (2004).
13. Hodgson, D.M. *et al.* Stable benefit of embryonic stem cell therapy in myocardial infarction. *Am. J. Physiol. Heart Circ. Physiol.* **287**, H471–H479 (2004).
14. Makino, S. *et al.* Cardiomyocytes can be generated from marrow stromal cells in vitro. *J. Clin. Invest.* **103**, 697–705 (1999).
15. Pittenger, M.F. *et al.* Multilineage potential of adult human mesenchymal stem cells. *Science* **284**, 143–147 (1999).
16. Reyes, M. *et al.* Origin of endothelial progenitors in human postnatal bone marrow. *J. Clin. Invest.* **109**, 337–346 (2002).
17. Toma, C., Pittenger, M.F., Cahill, K.S., Byrne, B.J. & Kessler, P.D. Human mesenchymal stem cells differentiate to a cardiomyocyte phenotype in the adult murine heart. *Circulation* **105**, 93–98 (2002).
18. Wang, J.S. *et al.* Marrow stromal cells for cellular cardiomyoplasty: feasibility and potential clinical advantages. *J. Thorac. Cardiovasc. Surg.* **120**, 999–1005 (2000).
19. Jiang, Y. *et al.* Pluripotency of mesenchymal stem cells derived from adult marrow. *Nature* **418**, 41–49 (2002).
20. Nagaya, N. *et al.* Transplantation of mesenchymal stem cells improves cardiac function in a rat model of dilated cardiomyopathy. *Circulation* **112**, 1128–1135 (2005).
21. Rangappa, S., Fen, C., Lee, E.H., Bongso, A. & Wei, E.S. Transformation of adult mesenchymal stem cells isolated from the fatty tissue into cardiomyocytes. *Ann. Thorac. Surg.* **75**, 775–779 (2003).
22. Zuk, P.A. *et al.* Human adipose tissue is a source of multipotent stem cells. *Mol. Biol. Cell* **13**, 4279–4295 (2002).
23. Gaustad, K.G., Boquest, A.C., Anderson, B.E., Gerdes, A.M. & Collas, P. Differentiation of human adipose tissue stem cells using extracts of rat cardiomyocytes. *Biochem. Biophys. Res. Commun.* **314**, 420–427 (2004).
24. Planat-Benard, V. *et al.* Plasticity of human adipose lineage cells toward endothelial cells: physiological and therapeutic perspectives. *Circulation* **109**, 656–663 (2004).
25. Lee, R.H. *et al.* Characterization and expression analysis of mesenchymal stem cells from human bone marrow and adipose tissue. *Cell. Physiol. Biochem.* **14**, 311–324 (2004).
26. Li, J., Takaishi, K., Cook, W., McCorkle, S.K. & Unger, R.H. Insig-1 "brakes" lipogenesis in adipocytes and inhibits differentiation of preadipocytes. *Proc. Natl. Acad. Sci. USA* **100**, 9476–9481 (2003).
27. Vande Berg, J.S., Rudolph, R. & Woodward, M. Comparative growth dynamics and morphology between cultured myofibroblasts from granulating wounds and dermal fibroblasts. *Am. J. Pathol.* **114**, 187–200 (1984).
28. Nishida, K. *et al.* Corneal reconstruction with tissue-engineered cell sheets composed of autologous oral mucosal epithelium. *N. Engl. J. Med.* **351**, 1187–1196 (2004).
29. Shimizu, T., Yamato, M., Kikuchi, A. & Okano, T. Cell sheet engineering for myocardial tissue reconstruction. *Biomaterials* **24**, 2309–2316 (2003).
30. Nishikimi, T., Uchino, K. & Frohlich, E.D. Effects of α1-adrenergic blockade on intrarenal hemodynamics in heart failure rats. *Am. J. Physiol. Regul. Integr. Comp. Physiol.* **262**, R198–R203 (1998).

Available online at www.sciencedirect.com
ScienceDirect
Neurochemistry International 49 (2006) 448–453
NEUROCHEMISTRY International
www.elsevier.com/locate/neuint

Effect of sustained limb ischemia on norepinephrine release from skeletal muscle sympathetic nerve endings

Yosuke Kuroko [a], Noriyuki Tokunaga [b], Toji Yamazaki [b,*], Tsuyoshi Akiyama [b], Kozo Ishino [a], Shunji Sano [a], Hidezo Mori [b]

[a] *Department of Cardiovascular Surgery, Okayama University Graduate School of Medicine and Dentistry, Okayama 700-8558, Japan*
[b] *Department of Cardiac Physiology, National Cardiovascular Center Research Institute, 5-7-1 Fujishiro-dai, Suita, Osaka 565-8565, Japan*

Received 8 October 2005; accepted 2 March 2006
Available online 24 April 2006

Abstract

Acute ischemia has been reported to impair sympathetic outflow distal to the ischemic area in various organs, whereas relatively little is known about this phenomenon in skeletal muscle. We examined how acute ischemia affects norepinephrine (NE) release at skeletal muscle sympathetic nerve endings. We implanted a dialysis probe into the adductor muscle in anesthetized rabbits and measured dialysate NE levels as an index of skeletal muscle interstitial NE levels. Regional ischemia was introduced by microsphere injection and ligation of the common iliac artery. The time courses of dialysate NE levels were examined during prolonged ischemia. Ischemia induced a decrease in the dialysate NE level (from 19 ± 4 to 2.0 ± 0 pg/ml, mean ± S.E.), and then a progressive increase in the dialysate NE level. The increment in the dialysate NE level was examined with local administration of desipramine (DMI, a membrane NE transport inhibitor), ω-conotoxin GVIA (CTX, an N-type Ca^{2+} channel blocker), or TMB-8 (an intracellular Ca^{2+} antagonist). At 4 h ischemia, the increment in the dialysate NE level (vehicle group, 143 ± 30 pg/ml) was suppressed by TMB-8 (25 ± 5 pg/ml) but not by DMI (128 ± 10 pg/ml) or CTX (122 ± 18 pg/ml). At 6 h ischemia, the increment in the dialysate NE level was not suppressed by the pretreatment. Ischemia induced biphasic responses in the skeletal muscle. Initial reduction of NE release may be mediated by an impairment of axonal conduction and/or NE release function, while in the later phase, the skeletal muscle ischemia-induced NE release was partly attributable to exocytosis via intracellular Ca^{2+} overload rather than opening of calcium channels or carrier mediated outward transport of NE.

Keywords: Catecholamine; Interstitial space; Microdialysis; Rabbit; Striate muscle

1. Introduction

Acute ischemia has been reported to be associated with impairment of the sympathetic tract (Schömig et al., 1984; Toyohara et al., 1986; Fujii et al., 2003). A well-known example is myocardial ischemia associated with impairment of the regional cardiac sympathetic nerve endings (Schömig et al., 1984; Ciuffo et al., 1985). Outward norepinephrine (NE) transport through uptake$_1$ carrier has been proposed as one of the main mechanisms responsible for ischemia-induced NE efflux from sympathetic nerve endings (Schömig et al., 1984; Akiyama and Yamazaki, 2001). However, little is known about the sympathetic impairment evoked by skeletal muscle ischemia. Histochemical and electrophysiological studies (Barker and Saito, 1981; Hill et al., 1996) have identified sympathetic innervation in skeletal muscle, which exerted actions on the regulation of regional blood flow and glucose metabolism (Thompson and Mohrman, 1983; Fagius and Berne, 1994). During and after exercise, muscle sympathetic nerve activity has been reported to be modulated by ischemia-induced metaboreceptor stimulation (Comett et al., 2000; Cui et al., 2001). Furthermore, skeletal muscle may be exposed to prolonged severe ischemia (Welsh and Lindinger, 1993). Severe skeletal muscle ischemia occurs with trauma, vascular diseases, and compartment syndrome. It is so far unknown whether severe muscle ischemia induces excessive NE release from muscle sympathetic nerve endings.

In view of energy metabolism, cardiac ischemia is characterized by rapid deterioration of cardiac function, which has been linked to a fall in intracellular pH, increased levels of inorganic phosphate and reduction in free energy changes of ATP-hydrolysis (Mair, 1999). In contrast to cardiac muscle,

* Corresponding author. Tel.: +81 6 6833 5012; fax: +81 6 6872 8092.
E-mail address: yamazaki@ri.ncvc.go.jp (T. Yamazaki).

0197-0186/$ – see front matter © 2006 Elsevier Ltd. All rights reserved.
doi:10.1016/j.neuint.2006.03.004

energy requirements in skeletal muscle are dependent on exercise and are reduced in the resting state since only resting tone is maintained (Idström et al., 1990; Lindsay et al., 1990). Typically, prolonged skeletal muscle ischemia imposes a metabolic stress that results in a depletion of glycogen, high-energy phosphagen, and adenine nucleotides (Welsh and Lindinger, 1993). Thus, a differential time course of energy metabolism occurs in the skeletal muscle and cardiac myocardium. No studies have systematically characterized the impairment of sympathetic nerves in the skeletal muscle ischemia.

Recently, we reported that microdialysis technique with high-performance liquid chromatography is a sensitive and versatile method for monitoring interstitial NE concentrations in myocardial ischemic regions (Akiyama et al., 1991, 1993). Moreover, we applied microdialysis technique to skeletal muscle and have reported that skeletal muscle dialysate NE serves as an index of muscle sympathetic nerve activity (Tokunaga et al., 2003a). Using this method, we investigated how acute skeletal muscle ischemia affects NE release from skeletal muscle sympathetic nerve endings and the mechanism of skeletal muscle ischemia-induced NE release with regional pharmacological intervention.

2. Methods

2.1. Animal model

The investigation conformed with the *Guide for the Care and Use of Laboratory Animals* published by the US National Institutes of Health (NIH Publication No. 85-23, revised 1996). Forty-two male Japanese white rabbits weighing 2.2–3.8 kg were used for the model of skeletal muscle ischemia. The animals were anesthetized with pentobarbital sodium (30–35 mg/kg) and ventilated with room air mixed with oxygen. The level of anesthesia was maintained with a continuous intravenous infusion of pentobarbital sodium (1–2 mg/kg/h). Body temperature was maintained with a heated pad and lamp. An electrocardiogram, heart rate (HR), and mean arterial blood pressure (MAP) were simultaneously monitored with a data recorder. After a longitudinal skin incision was made in the left groin, the dialysis probes were implanted in the left adductor muscle with a fine guiding needle.

2.2. Dialysis technique and NE measurements

With the dialysis technique, dialysate NE levels were measured as an index of skeletal muscle interstitial NE levels. For skeletal muscle dialysis, we designed a transverse dialysis probe. The dialysis fiber (13 mm length, 0.31 mm o.d. and 0.2 mm i.d.; PAN-1200, 50,000 molecular mass cut-off, Asahi Chemical, Tokyo, Japan) was glued at both ends into a polyethylene tube (25 cm length, 0.5 mm o.d. and 0.2 mm i.d.) (Akiyama et al., 1991). The dialysis probe was perfused with Ringer solution using a microinjection pump (CMA 102, Camergie Medicin, Stockholm, Sweden). Similar to previous studies (Tokunaga et al., 2003a, 2003b), we chose a perfusion speed of 10 μl/min for skeletal muscle. Sampling periods were set at 15 min for skeletal muscle. Dialysate NE levels were measured by high-performance liquid chromatography with electrochemical detection (ECD-300, Eicom, Kyoto, Japan) after removing interfering compounds in the dialysate by an alumina procedure (Anton and Sayer, 1962; Akiyama et al., 1991). Dialysate dihydroxyphenylglycol (DHPG) levels were measured by separate high-performance liquid chromatography with electrochemical detection (Akiyama and Yamazaki, 2001).

2.3. Experimental protocols

Acute skeletal muscle ischemia was induced by injection of non-radioactive iodine-labeled microspheres (15 μm in diameter, 3 × 10^7/kg, Sekisui Plastic, Osaka, Japan) through the left common iliac artery, as previously described (Tanaka et al., 2000). After the injection of microspheres, the common iliac artery was ligated.

2.3.1. Protocol 1: time courses of dialysate NE levels during acute ischemia

To examine the time courses of dialysate NE levels during acute skeletal muscle ischemia, we measured dialysate NE levels over 60-min periods of skeletal muscle ischemia ($n = 6$). We collected four consecutive 15-min dialysate samples. Furthermore, we measured dialysate NE samples over a period of 6 h of skeletal muscle ischemia with 2 h interval in separate rabbits. To examine intraneuronal NE kinetics in the skeletal muscle, the measurement of dialysate DHPG level was added during 6 h of skeletal muscle ischemia ($n = 6$).

2.3.2. Protocol 2: involvement of NE uptake$_1$ transport, Ca^{2+} channels and cytosol Ca^{2+} in dialysate NE levels during acute ischemia

To examine the mechanism underlying the increment of NE release during the prolonged ischemia, dialysate NE levels were measured with regional pharmacological intervention. Neurotransmitter release from sympathetic nerve endings can be caused by a variety of different mechanisms (Schömig et al., 1987; Kawada et al., 2000; Akiyama and Yamazaki, 2001). In the present studies, we examined the roles of membrane NE transport, N-type Ca^{2+} channels and cytosol Ca^{2+} in the time courses of dialysate NE levels during prolonged ischemia. To examine the involvement of membrane NE transport in the ischemia-induced NE release, we locally administered an uptake$_1$ carrier blocker, desipramine (100 μM) through a dialysis probe and observed the responses of dialysate NE (Akiyama and Yamazaki, 2001) ($n = 6$). The same protocol was performed with addition of a voltage-dependent N-type Ca^{2+} channel blocker, ω-conotoxin GVIA (10 μM) ($n = 6$) or intracellular Ca^{2+} antagonist, 8-(*N*,*N*-diethylamino)-octyl-3,4,5-trimethoxybenzoate hydrochloride (TMB-8, 1 mM) ($n = 6$) through a dialysis probe. From data on protocol 1, we observed increases in dialysate NE levels after 2 h of skeletal muscle ischemia. Therefore, the time course of dialysate NE for skeletal muscle ischemia was examined over a period of 6 h with a 2 h-interval ($n = 6$). The effectiveness of ω-conotoxin GVIA (10 μM) ($n = 6$) or TMB-8 (1 mM) ($n = 6$) was tested before the experiment in separate rabbits. We administered high potassium (KCl, 100 mM) locally through the dialysis probe, and the dialysate NE response was obtained in the presence and absence of ω-conotoxin GVIA or TMB-8. High-K increased dialysate NE from 11.7 ± 2.8 to 84.7 ± 20.8 pg/ml ($n = 6$). This KCl-induced increment in dialysate NE was attenuated by the addition of ω-conotoxin GVIA or TMB-8 (Fig. 1).

2.3.3. Protocol 3: time courses of dialysate lactate levels during the hind limb ischemia

To confirm whether this perturbation induces tissue ischemia, we examined the time course of dialysate lactate levels as an index of tissue ischemia. The dialysate lactate levels were measured by kinetic enzymatic analysis with CMA 600 (Carnegie Medicin). In the skeletal muscle ischemia, four consecutive 15-

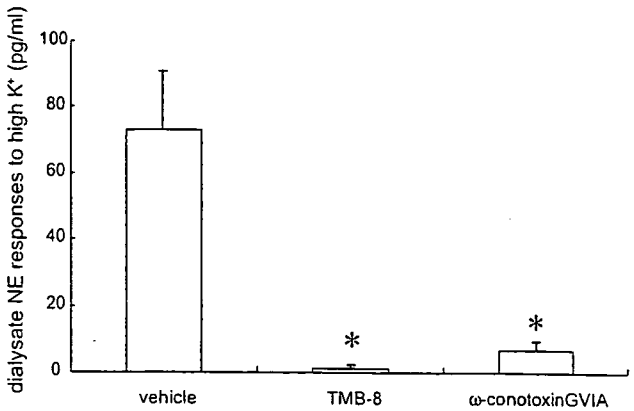

Fig. 1. Effects of pharmacological intervention on dialysate norepinephrine (NE) responses to high K^+ (KCl, 100 mM). Both TMB-8 (1 mM) and ω-conotoxin (10 μM) suppressed dialysate responses to high K^+. Values are means ± S.E. ($n = 6$).

min dialysate samples were collected during the initial 60-min and subsequently three consecutive samples were collected over a period of 6 h with a 2 h-interval ($n = 6$).

2.4. Statistical analysis

All data are presented as mean ± S.E. values. Hemodynamic and dialysate data responses to acute ischemia were statistically analyzed by analysis of variance with repeated measures. When a statistically significant effect of ischemia was detected as a whole, the Dunnett's test was applied to determine which mean values differed significantly from the control level. When a statistically significant effect of the treatment was detected, Newman–Keuls test was applied to determine which treatment differed significantly from the vehicle.

3. Results

Table 1 summarizes changes in HR and MAP. MAP and HR increased during 6 h-hind limb ischemia. Changes in MAP at 2 h and HR at 6 h-hind limb ischemia were significant.

3.1. Time courses of dialysate NE levels during short and prolonged ischemia

Skeletal muscle dialysate NE levels decreased from 19 ± 4 pg/ml at control to 9 ± 4 pg/ml at 30 min of ischemia and reached 2 ± 0 pg/ml at 60 min of ischemia (Fig. 2). The decrease in dialysate NE level was maintained after 2 h of ischemia. Then skeletal muscle dialysate NE levels markedly increased to 143 ± 30 pg/ml at 4 h of ischemia. The dialysate NE levels continued to increase progressively and reached 289 ± 45 pg/ml at 6 h of ischemia. Skeletal muscle dialysate DHPG levels decreased from 38 ± 2 pg/ml at control to 5 ± 1 pg/ml at 2 h of ischemia and reached 7 ± 1 pg/ml at 6 h of ischemia.

3.2. Involvement of NE uptake$_1$ transport, Ca^{2+} channels and cytosol Ca^{2+} in dialysate NE levels during prolonged ischemia

Dialysate NE increases at 4 and 6 h-skeletal muscle ischemia were not suppressed by treatment with desipramine (Fig. 3). Dialysate NE increases at 4 and 6 h-skeletal muscle ischemia were not suppressed by treatment with ω-conotoxin GVIA. Treatment with TMB-8 significantly suppressed the dialysate NE increase at 4 h-skeletal muscle ischemia. But at 6 h-skeletal muscle ischemia, there was no significant difference in dialysate NE levels among treatments.

Table 1
Changes in heart rate (HR) and mean arterial pressure (MAP) in 6 h-hindlimb ischemia

	Control	2 h	4 h	6 h
HR (beats/min)	283 ± 10	292 ± 4	293 ± 8	302 ± 8*
MAP (mmHg)	104 ± 6	114 ± 3*	111 ± 4	108 ± 4

Values are means ± S.E. from six rabbits. Data were obtained during control, after 2, 4, and 6 h of hind limb ischemia.
* $P < 0.05$ vs. control.

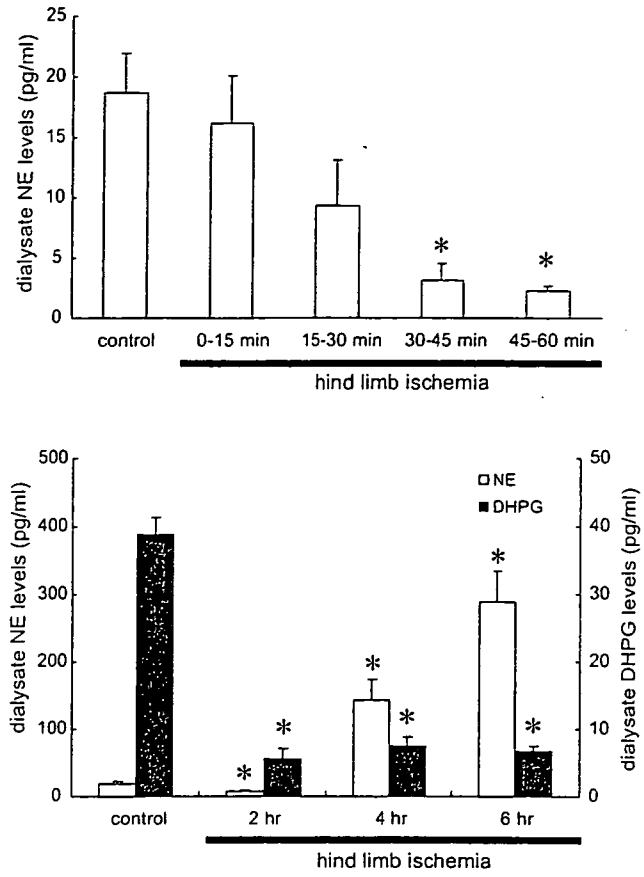

Fig. 2. (Upper panel) Time course of dialysate norepinephrine (NE) levels during 60 min-hind limb ischemia. Values are means ± S.E. ($n = 6$). *$P < 0.05$ vs. control value. (Lower panel) Time courses of dialysate NE and dihydroxyphenylglycol (DHPG) levels during 6 h-hind limb ischemia. Values are means ± S.E. ($n = 6$). *$P < 0.05$ vs. control value.

3.3. Time course of dialysate lactate levels during hind limb ischemia

Skeletal muscle dialysate lactate levels increased from 0.6 ± 0.07 nmol/l at control to 1.73 ± 0.17 nmol/l at 45–60 min

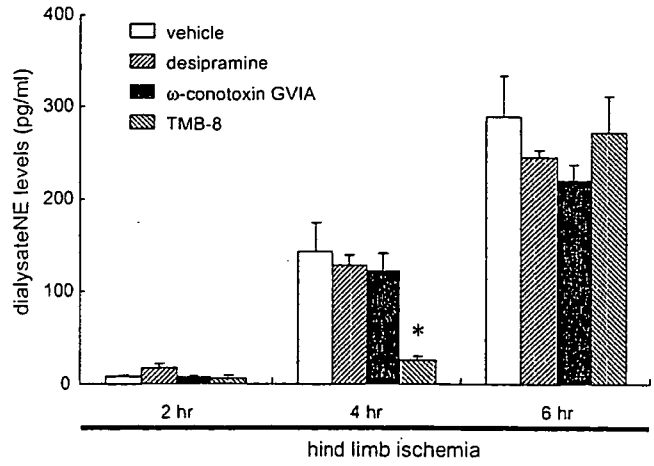

Fig. 3. Effects of pharmacological intervention on dialysate norepinephrine (NE) levels evoked by 6 h-hind limb ischemia. Desipramine (100 μM), ω-conotoxin (10 μM), or TMB-8 (1mM) was locally administered through the probe. Values are means ± S.E. ($n = 6$). *$P < 0.05$ vs. concurrent value of vehicle group.

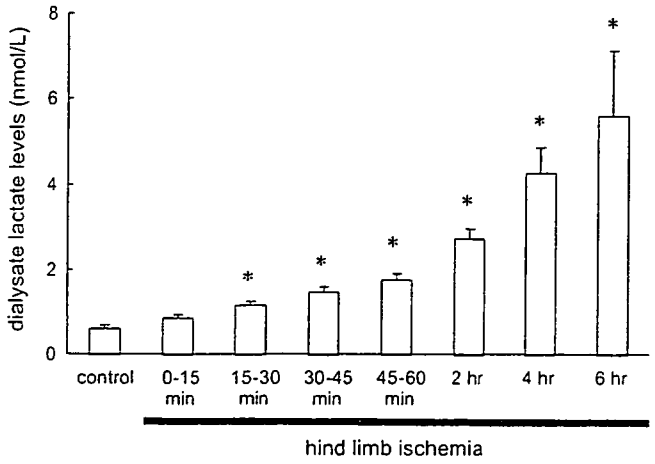

Fig. 4. Time course of dialysate lactate levels during 6 h-hind limb ischemia. Values are means ± S.E. ($n = 6$). $^{*}P < 0.05$ vs. control value.

of ischemia (Fig. 4). These step-wise increases were continued for 6 h of the hind limb ischemia.

4. Discussion

Using dialysis techniques in the in vivo rabbit skeletal muscle, we examined interstitial levels of NE in the control and ischemic period, and observed the biphasic response of dialysate NE in ischemic skeletal muscle. Ischemia induced an initial reduction followed by a progressive increment in dialysate NE levels. Here we discuss changes in interstitial NE and possible mechanisms underlying sympathetic nerve impairment.

Within 2 h of acute skeletal muscle ischemia, unlike acute myocardial ischemia, skeletal muscle interstitial NE levels continued to decline progressively, decreasing to one-tenth of control at 60 min of ischemia. A previous study demonstrated that skeletal muscle ischemia modulated the baroreflex control of regional muscle sympathetic activity (Cornett et al., 2000). At 75 min of acute skeletal muscle ischemia, hemodynamic responses to carotid occlusion were preserved while the interstitial NE response to carotid occlusion was blunted in the ischemic region (Tokunaga et al., 2003b). These results indicate that the systemic response to baroreflex remained intact while the skeletal muscle sympathetic response was impaired in ischemic regions. Earlier studies reported that acute limb ischemia reduced the conduction of motor nerves such as sciatic nerve (Fern and Harrison, 1994), and induced axonal degeneration histologically (Makitie and Teravainen, 1977; Nukada and Dyek, 1987). Axonal conduction in the ischemic muscle sympathetic nerve may be impaired as well as in sensory and motor nerves. In addition to diminished axonal conductance, the interstitial NE response to high K^+ but not tyramine was suppressed during the 75 min of acute skeletal muscle ischemia, although NE content at muscle sympathetic nerve endings was preserved during the ischemia (Tokunaga et al., 2003b). This result indicates that exocytotic NE releasing function in muscle sympathetic nerve endings might be suppressed during 75 min of acute skeletal muscle ischemia. Therefore, initial reduction of NE release may be mediated by an impairment of axonal conduction and/or NE releasing function.

After 2 h of acute skeletal muscle ischemia, skeletal muscle interstitial NE levels significantly increased and finally reached 20-fold that of control. This amount of NE release is higher than that evoked by baroreflex or high K^+. This level is similar to that evoked by the Na^+–K^+ ATPase inhibitor, ouabain (Tokunaga et al., 2003a). The amount of NE release evoked by ischemia may be dependent on the density of sympathetic innervation. Dispersed organ systems such as skeletal muscle have a thin and diffuse sympathetic innervation. This is the first report to describe that marked NE release is induced from muscle sympathetic nerve endings in the ischemic region after 2 h of skeletal muscle ischemia. Numerous histological changes of skeletal muscle have been reported after ischemia and reperfusion injury (Patterson and Klenerman, 1979; Turchányi et al., 2005). However, there is no histochemical evidence of the impaired sympathetic nerves in the skeletal muscle ischemia.

In the case of skeletal muscle ischemia, ω-conotoxin GVIA did not suppress NE efflux. N-type Ca^{2+} channels are not involved in this NE efflux. Desipramine did not alter NE efflux during skeletal muscle ischemia. Desipramine inhibits carrier-mediated NE transport in both directions. Considering that desipramine did not alter interstitial NE levels, the amounts of NE release and uptake via normal transport can be surmised to be negligible. Second, the increase in skeletal muscle interstitial NE levels was not associated with an increase in skeletal muscle interstitial DHPG levels, indicating that skeletal ischemia fails to induce axoplasmic NE elevation via alterations in monoamine activity, NE mobilization from stored vesicle, and NE uptake. Further, desipramine did not suppress NE efflux. These results exclude the possibility that marked increases in skeletal muscle interstitial NE could be due to carrier-mediated outward transport of NE for removal of elevated axoplasmic NE concentration. The membrane NE transporter exists in the skeletal muscle sympathetic nerve endings (Cabassi et al., 2001; Tokunaga et al., 2003a), but was not involved in outward transport of NE. Thus, we consider that a ω-conotoxin GVIA insensitive and desipramine-resistant NE release mechanism exists after 2 h of acute skeletal muscle ischemia.

TMB-8 significantly suppressed the marked NE release at 4 h of skeletal muscle ischemia. TMB-8 is well known to inhibit Ca^{2+} release from intracellular Ca^{2+} stores. TMB-8 inhibits caffeine-induced catecholamine release from perfused adrenal gland in the absence of extracellular Ca^{2+} (Yamada et al., 1988). Studies using chromaffin cells, brain slices and synaptosomes have suggested that metabolic inhibition induces intracellular Ca^{2+} overload (Milusheva et al., 1992), and a rise in the intracellular Ca^{2+} causes exocytotic catecholamine release without membrane depolarization (Dry et al., 1991; Du et al., 1997). Moreover, an in vitro study with adrenergic nerves of guinea-pig vas deferens suggested that Ca^{2+} release from intracellular Ca^{2+} stores is to some extent involved in the NE release evoked by elevation of intracellular Na^+ (Katsuragi et al., 1994). Under energy-depleted conditions, Ca^{2+} overload

in synaptosomes of noradrenergic neurons from the brain is an important mechanism for the enhanced release of neurotransmitter, with a reversal of Na^+–Ca^{2+} exchange possibly the key pathway leading to intraneuronal Ca^{2+} overload (Du et al., 1997). We consider that Ca^{2+} release from intracellular Ca^{2+} stores is partly involved in the NE release at 4 h of skeletal muscle ischemia.

At 6 h of skeletal ischemia, increment in dialysate NE level was not suppressed by the pretreatments. This result suggests that another mechanism may be involved in NE release, which is insensitive to desipramine, ω-conotoxin GVIA, and TMB-8. Alternatively, the NE release may occur with development of irreversible membrane damage and can no longer be inhibited by pharmacological interventions. Future work should concentrate on these aspects of NE release during the later period.

4.1. Methodological considerations

The limitation of this experiment is related to the methodology and the duration of the hind limb ischemia. In a variety of these experimental models for organ ischemia, we chose microsphere injection and iliac artery occlusion for the short and prolonged hind limb ischemia model. A preliminary experiment indicated that common iliac artery occlusion did not yield severe ischemia or muscle necrosis in a chronic ischemic model because collateral flow prevents skeletal muscle ischemia. The combination of artery occlusion and injection of microsphere was used for the hind limb ischemic model. In the hind limb ischemia, however, we did not measure skeletal muscle blood flow. To confirm whether this perturbation induced reduction of blood flow and tissue ischemia, we measured dialysate lactate levels in skeletal muscle as an index of tissue ischemia. This perturbation induced increases in dialysate lactate levels. In the present study, dialysate NE responses were examined in prolonged 6 h ischemia. Temporal changes in MAP and HR appeared but sustained significant hemodynamic changes were not observed. This duration was referred to the experiments on the tourniquet application and release time (Sapega et al., 1985; Mitrev et al., 1996). Four to 6 h of ischemic periods has been thought to produce extensive and reversible damage of skeletal muscle. Therefore, data on pharmacological intervention were obtained within 6 h of skeletal muscle ischemia.

Ischemia induced biphasic NE responses in the skeletal muscle. Initial reduction of NE release may be mediated by an impairment of axonal conduction and/or NE releasing function, while in the later phase, the skeletal muscle ischemia-induced NE release was partly attributable to exocytosis via intracellular Ca^{2+} overload rather than opening of calcium channels or carrier mediated outward transport of NE.

Acknowledgements

This study was supported by Grants-in Aid for scientific research (15590787) from the Ministry of Education, Culture, Sports, Science and Technology; the Research Grants for Cardiovascular Disease (H13C-1) from the Ministry of Health, Labor and Welfare.

References

Akiyama, T., Yamazaki, T., Ninomiya, I., 1991. In vivo monitoring of myocardial interstitial norepinephrine by dialysis technique. Am. J. Physiol. 261, H1643–H1647.

Akiyama, T., Yamazaki, T., Ninomiya, I., 1993. Differential regional responses of myocardial interstitial noradrenaline levels to coronary occlusion. Cardiovasc. Res. 27, 817–822.

Akiyama, T., Yamazaki, T., 2001. Myocardial interstitial norepinephrine and dihydroxyphenylglycol levels during ischemia and reperfusion. Cardiovasc. Res. 49, 78–85.

Anton, A.H., Sayer, D.F., 1962. A study of the factors affecting the aluminum oxide-trihydroxyindole procedure for the analysis of catecholamine. J. Pharmacol. Exp. Ther. 138, 360–375.

Barker, D., Saito, M., 1981. Autonomic innervation of receptors and muscle fibers in cat skeletal muscle. Proc. Roy. Soc. Lond., B: Biol. Sci. 212, 317–332.

Cabassi, A., Vinci, S., Quartieri, F., Moschini, L., Borghetti, A., 2001. Norepinephrine uptake is impaired in skeletal muscle of hypertensive rats in vivo. Hypertension 37, 698–702.

Ciuffo, A.A., Ouyang, P., Becker, L.C., Levin, L., Weisfeldt, M.L., 1985. Reduction of sympathetic inotropic response after ischemia in dogs. Contributor to stunned myocardium. J. Clin. Invest. 75, 1504–1509.

Cornett, J.A., Herr, M.D., Gray, K.S., Smith, M.B., Yang, Q.X., Sinoway, L.I., 2000. Ischemic exercise and the muscle metaboreflex. J. Appl. Physiol. 89, 1432–1436.

Cui, J., Wilson, T.E., Shibasaki, M., Hodges, N.A., Grandall, C.G., 2001. Baroreflex modulation of muscle sympathetic nerve activity during postgrip muscle ischemia in human. J. Appl. Physiol. 91, 1679–1686.

Dry, K.L., Phillips, J.H., Dart, A.M., 1991. Catecholamine release from bovine adrenal chromaffin cells during anoxia or metabolic inhibition. Circ. Res. 69, 466–474.

Du, X.-J., Bobik, A., Little, P.J., Esler, M.D., Dart, A.M., 1997. Role of Ca^{2+} in metabolic inhibition-induced norepinephrine release in rat brain synaptosomes. Circ. Res. 80, 179–188.

Fagius, J., Berne, C., 1994. Increase in muscle sympathetic activity in humans after food intake. Clin. Sci. (London) 86, 159–167.

Fern, R., Harrison, P.J., 1994. The relationship between ischaemic conduction failure and conduction velocity in cat myelinated axons. Exp. Physiol. 79, 571–581.

Fujii, T., Kurata, H., Takaoka, M., Muraoka, T., Fujisawa, Y., Shokoji, T., Nishiyama, A., Abe, Y., Matsumura, Y., 2003. The role of renal sympathetic nervous system in the pathogenesis of ischemic acute renal failure. Eur. J. Pharmacol. 481, 241–248.

Hill, J.M., Adreani, C.M., Kaufman, M.P., 1996. Muscle reflex stimulates sympathetic postganglionic efferents innervating triceps surae muscle of cats. Am. J. Physiol. 271, H38–H43.

Idström, J.-P., Soussi, B., Elander, A., Bylund-Fellenius, A.-C., 1990. Purine metabolism after in vivo ischemia and reperfusion in rat skeletal muscle. Am. J. Physiol. 258, H1668–H1673.

Katsuragi, T., Ogawa, S., Furukawa, T., 1994. Contribution of intra- and extracellular Ca^{2+} to noradrenaline exocytosis induced by ouabain and monensin from guinea-pig vas deferens. Br. J. Pharmacol. 113, 795–800.

Kawada, T., Yamazaki, T., Akiyama, T., Sato, T., Shishido, T., Inagaki, M., Tetewaki, T., Yanagiya, Y., Sugimachi, M., Sunagawa, K., 2000. Cyanide intoxication induced exocytotic epinephrine release in rabbit myocardium. J. Auton. Nerv. Syst. 80, 137–141.

Lindsay, T.F., Liauw, S., Romaschin, A.D., Walker, P.M., 1990. The effect of ischemia/reperfusion on adenine nucleotide metabolism and xanthine oxidase production in skeletal muscle. J. Vasc. Surg. 12, 8–15.

Mair, J., 1999. Tissue release of cardiac markers: from physiology to clinical applications. Clin. Chem. Lab. Med. 37, 1077–1084.

Makitie, J., Teravainen, H., 1977. Peripheral nerve injury and recovery after temporary ischemia. Acta Neuropathol. (Berl.) 37, 55–63.

Milusheva, E., Doda, M., Pasztor, E., Lajtha, A., Sershen, H., Vizi, E.S., 1992. Regulatory interactions among axonal terminals affecting the release of different transmitters from rat striatal slices under hypoxic and hypoglycemic conditions. J. Neurochem. 59, 946–952.

Mitrev, Z., Ihnken, K., Poloczek, Y., Hallmann, R., Herold, H., Unkelbach, U., Zimmer, G., Freisleben, H.J., Beyersdorf, S., Beyersdorf, F., 1996. Controlled reperfusion of the extremities for preventing local and systemic damage after prolonged ischemia. An experimental study with the swine model. Zentralbl. Chir. 121, 774–787.

Nukada, H., Dyek, P.J., 1987. Acute ischemia causes axonal stasis, swelling, attenuation and secondary demyelination. Ann. Neurol. 22, 311–318.

Patterson, S., Klenerman, 1979. The effect of pneumatic tourniquets on the ultrastructure of skeletal muscle. J. Bone Joint Surg. Br. 61, 178–183.

Schömig, A., Dart, A.M., Dietz, R., Mayer, E., Kubler, W., 1984. Release of endogenous catecholamines in the ischemic myocardium of the rat. Part A. Locally mediated release. Circ. Res. 55, 689–701.

Schömig, A., Fischer, S., Kurz, T., Richardt, G., Schömig, E., 1987. Non-exocytotic release of endogenous noradrenaline in the ischemic and anoxic rat heart: mechanism and metabolic requirements. Circ. Res. 60, 194–205.

Sapega, A.A., Heppenstall, R.B., Chance, B., Park, Y.S., Sokolow, D., 1985. Optimizing tourniquet application and release times in extremity surgery. A biochemical and ultrastructual study. J. Bone Joint Surg. Am. 67, 303–314.

Tanaka, E., Hattan, N., Ando, K., Ueno, H., Sugio, Y., Mohammed, M.U., Voltchikhina, S.A., Mori, H., 2000. Amelioration of microvascular myocardial ischemia by gene transfer of vascular endothelial growth factor in rabbits. J. Thorac. Cardiovasc. Surg. 120, 720–728.

Thompson, L.P., Mohrman, D.E., 1983. Blood flow and oxygen consumption in skeletal muscle during sympathetic stimulation. Am. J. Physiol. 245, H66–H71.

Tokunaga, N., Yamazaki, T., Akiyama, T., Sano, S., Mori, H., 2003a. In vivo monitoring of norepinephrine and its metabolites in skeletal muscle. Neurochem. Int. 43, 573–580.

Tokunaga, N., Yamazaki, T., Akiyama, T., Sano, S., Mori, H., 2003b. Acute limb ischemia does not facilitate but inhibits norepinephrine release from sympathetic nerve endings in anesthetized rabbit. J. Cardiovasc. Pharmacol. 42, S7–S10.

Toyohara, T., Nada, O., Ikeda, K., 1986. Influence of ischemia on noradrenergic nerves in the terminal colon of humans and rats. Eur. Surg. Res. 18, 349–355.

Turchányi, B., Tóth, B., Rácz, I., Vendégh, Z., Fűrész, J., Hamar, J., 2005. Ischemia reperfusion injury of the skeletal muscle after selective deafferentation. Physiol. Res. 54, 25–31.

Welsh, D.G., Lindinger, M.I., 1993. Energy metabolism and adenine nucleotide degradation in twitch-stimulated rat hindlimb during ischemia-reperfusion. Am. J. Physiol. 264, E655–E661.

Yamada, Y., Teraoka, H., Nakazato, Y., Ohga, A., 1988. Intracellular Ca^{2+} antagonist TMB-8 blocks catecholamine secretion evoked by caffeine and acetylcholine from perfused cat adrenal glands in the absence of extracellular Ca^{2+}. Neurosci. Lett. 90, 338–342.

Available online at www.sciencedirect.com
ScienceDirect
Radiation Physics and Chemistry 75 (2006) 2008–2013
Radiation Physics and Chemistry
www.elsevier.com/locate/radphyschem

Tunable narrow-photon-energy X-ray generator utilizing a tungsten-target tube

Eiichi Sato[a,*], Hiroshi Sugiyama[b], Masami Ando[b], Etsuro Tanaka[c], Hidezo Mori[d], Toshiaki Kawai[e], Takashi Inoue[f], Akira Ogawa[f], Kazuyoshi Takayama[g], Jun Onagawa[h], Hideaki Ido[h]

[a]*Department of Physics, Iwate Medical University, 3-16-1 Honchodori, Morioka 020-0015, Japan*
[b]*Photon Factory, Institute of Materials Structure Science, High Energy Accelerator Research Organization, 1-1 Oho, Tsukuba 305-0801, Japan*
[c]*Department of Nutritional Science, Faculty of Applied Bio-science, Tokyo University of Agriculture, 1-1-1 Sakuragaoka, Setagaya-ku 156-8502, Japan*
[d]*Department of Cardiac Physiology, National Cardiovascular Center Research Institute, 5-7-1 Fujishirodai, Suita, Osaka 565-8565 Japan*
[e]*Electron Tube Division #2, Hamamatsu Photonics K.K., 314-5 Shimokanzo, Iwata 438-0193, Japan*
[f]*Department of Neurosurgery, School of Medicine, Iwate Medical University, 19-1 Uchimaru, Morioka 020-8505, Japan*
[g]*Shock Wave Research Center, Institute of Fluid Science, Tohoku University, 2-1-1 Katahira, Sendai 980-8577, Japan*
[h]*Department of Applied Physics and Informatics, Faculty of Engineering, Tohoku Gakuin University, 1-13-1 Chuo, Tagajo 985-8537, Japan*

Accepted 23 November 2005

Abstract

A preliminary experiment for producing narrow-photon-energy cone-beam X-rays using a silicon single crystal is described. In order to produce low-photon-energy X-rays, a 100-μm-focus X-ray generator in conjunction with a (1 1 1) plane silicon crystal is employed. The X-ray generator consists of a main controller and a unit with a high-voltage circuit and a microfocus X-ray tube. The maximum tube voltage and current were 35 kV and 0.50 mA, respectively, and the X-ray intensity of the microfocus generator was 48.3 μGy/s at 1.0 m from the source with a tube voltage of 30 kV and a current of 0.50 mA. The effective photon energy is determined by Bragg's angle, and the photon-energy width is regulated by the angle delta. Using this generator in conjunction with a computed radiography system, quasi-monochromatic radiography was performed using a cone beam with an effective energy of approximately 17 keV.

PACS: 87.59.−e; 87.59.Bh; 87.64.Gb

Keywords: Narrow-photon-energy X-rays; Tunable photon energy; Silicon single crystal; Cone beam

1. Introduction

Since the birth of the synchrotron, monochromatic parallel X-ray beams have been applied to X-ray phase-contrast radiography (Davis et al., 1995; Momose et al.,

*Corresponding author.
E-mail address: dresato@iwate-med.ac.jp (E. Sato).

0969-806X/$ - see front matter © 2006 Elsevier Ltd. All rights reserved.
doi:10.1016/j.radphyschem.2005.11.019

1996; Ando et al., 2002) and enhanced K-edge angiography (Thompson et al., 1992; Mori et al., 1996; Hyodo et al., 1998). The phase imaging is primarily based on the X-ray refraction, and the angiography is performed using X-rays with a photon energy of just beyond the K-absorption edge of iodine.

In order to perform high-speed medical radiography, although several different flash X-ray generators utilizing cold-cathode tubes have been developed (Sato et al., 1990, 1994a, b; Shikoda et al., 1994; Takahashi et al., 1994), quasi-monochromatic flash X-ray generators (Sato et al., 2003a, b, 2004a,b, 2005a–c) are useful to produce clean K-series characteristic X-rays without using a filter. Therefore, we have performed a demonstration of cone-beam K-edge angiography utilizing a cerium plasma generator, since K-series characteristic X-rays from the cerium target are absorbed effectively by iodine. In view of this situation, we have developed a steady state X-ray generator utilizing a cerium-target tube (Sato et al., 2004c), and have demonstrated enhanced K-edge angiography utilizing cerium Kα lines.

Without using synchrotrons, X-ray phase-contrast radiography for edge enhancement has been performed using a microfocus X-ray tube (Wilkins et al., 1996), and the digital imaging achieved with a 100-μm-focus molybdenum tube has been applied effectively to perform mammography (Ishisaka et al., 2000).

In this paper, we present a tunable narrow-photon-energy X-ray generator utilizing a single silicon crystal, and examine its suitability for energy-selective cone-beam radiography.

2. Experimental setup

Fig. 1 shows the block diagram of the X-ray generator, which consists of a main controller and an X-ray tube unit with a Cockcroft–Walton circuit and a 100-μm-focus X-ray tube. The tube voltage, the current, and the exposure time can be controlled by the controller. The main circuit for producing X-rays is illustrated in Fig. 2, and employed the Cockcroft–Walton circuit in order to decrease the dimensions of the tube unit. In the X-ray tube, positive and negative high voltages are applied to the anode and cathode electrodes, respectively. The filament heating current is supplied by an AC power supply in the controller in conjunction with an insulation transformer. The maximum tube voltage and current of the generator are 105 kV and 0.50 mA, respectively. In this experiment, the tube voltage applied was from 18 to 34 kV, and the tube current was 0.50 mA (maximum current) by the filament temperature. The exposure time is controlled in order to obtain optimum X-ray intensity.

The narrow-photon-energy X-ray generator utilizing a single silicon crystal of (1 1 1) plane is shown in Fig. 3. The effective photon energy is determined by Bragg's angle, and the photon-energy width is regulated by the

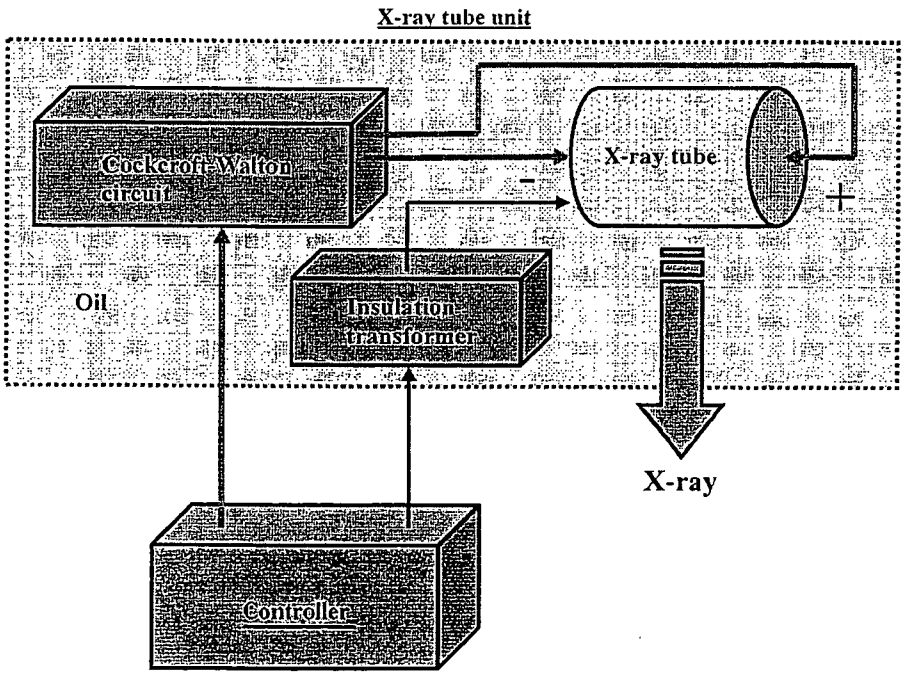

Fig. 1. Block diagram of a compact 100-μm focus X-ray generator with a tungsten-target radiation tube.

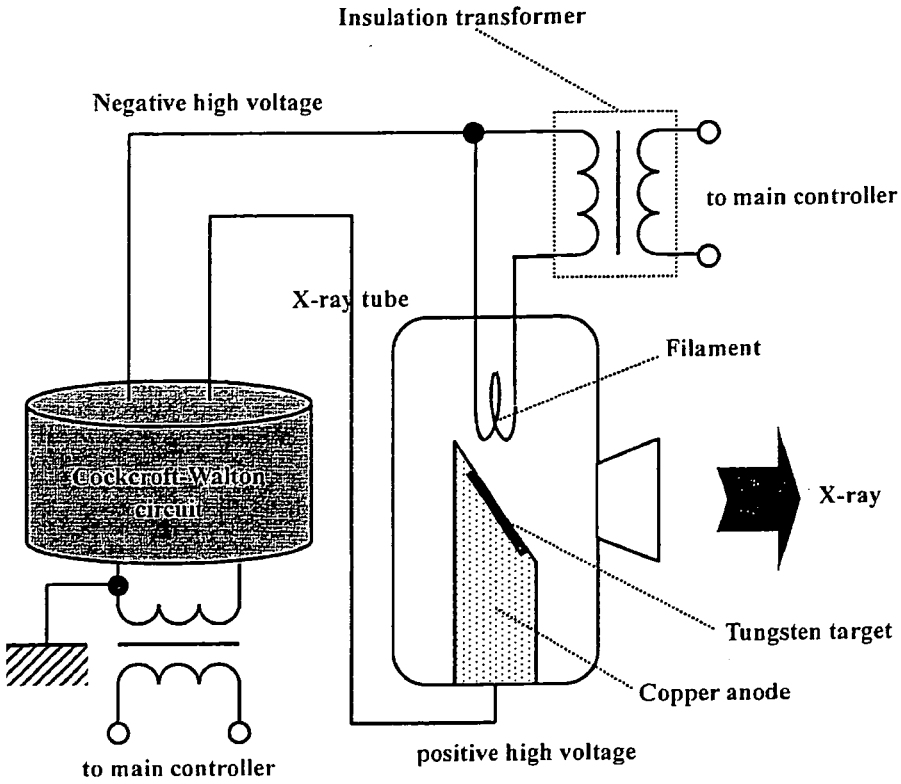

Fig. 2. Main circuit of the X-ray generator.

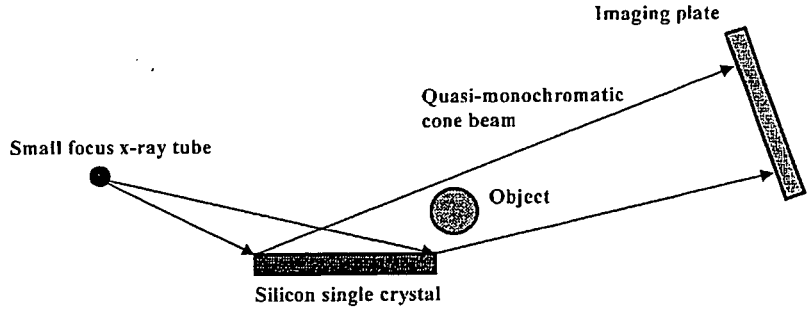

Fig. 3. Experimental setup of the narrow-photon-energy X-ray generator utilizing a single silicon crystal.

angle delta. Using this generator in conjunction with a computed radiography (CR) system (Sato et al., 2000), quasi-monochromatic radiography was performed using a cone beam with an effective energy of approximately 17 keV.

3. Results

3.1. X-ray intensity

X-ray intensity was measured by a Victoreen 660 ionization chamber at 1.0 m from the X-ray source (Fig. 4). At a constant tube current of 0.50 mA, the X-ray intensity increased when the tube voltage was increased. In this measurement, the intensity with a tube voltage of 30 kV was 48.3 μGy/s at 1.0 m from the source.

3.2. Radiography

The radiography was performed by the CR system (Konica Minolta Regius 150) with a sampling pitch of 87.5 μm, and the conditions for radiography were as in Fig. 3. Fig. 5 shows the irradiation field diffracted by the crystal with photon energies of approximately 17 keV.

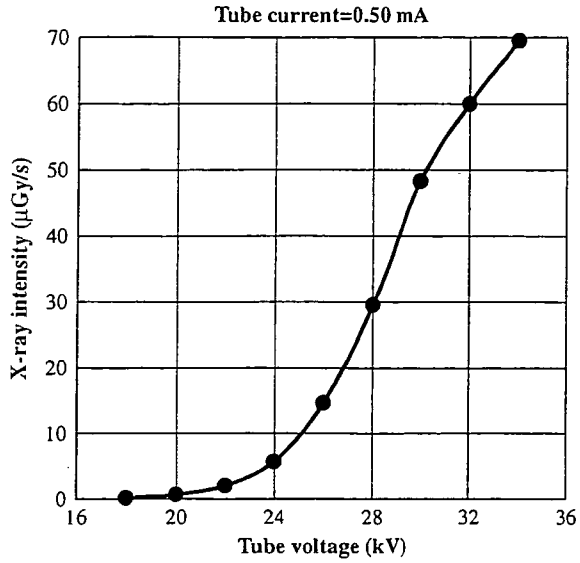

Fig. 4. X-ray intensity (μGy/s) as a function of tube voltage (kV) with a tube current of 0.50 mA.

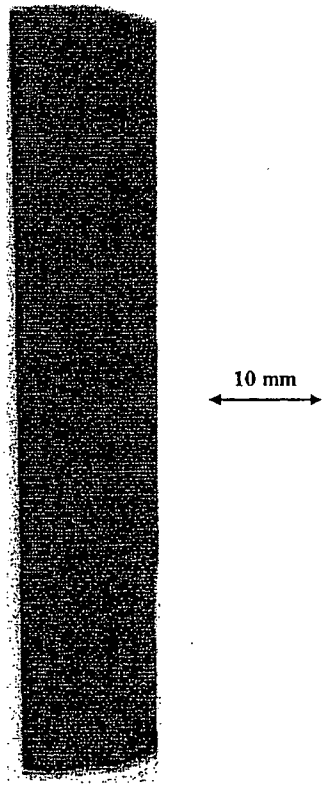

Fig. 5. Irradiation field with photon energies of approximately 17 keV measured using the CR system with a tube voltage of 30 kV.

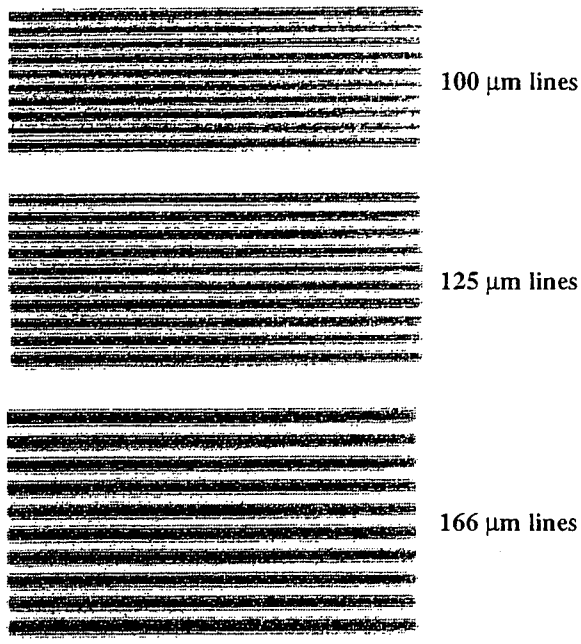

Fig. 6. Radiogram of a lead test chart for measuring the spatial resolution.

Because the width of the irradiation field was narrow due to the angle, the distance between the crystal and the imaging plate should be increased. Fig. 6 shows a radiogram of a test chart for determining the spatial resolution. In this radiography, 100-μm-wide lead lines (5 line pair) were observed. Subsequently, fine bone structures were visible in radiograms of a vertebra (Fig. 7), and fine blood vessels were observed in an angiogram of a rabbit heart (Fig. 8).

4. Conclusion and outlook

In summary, we employed a 100-μm-fosus X-ray generator with a tungsten-target tube and succeeded in producing narrow-photon-energy bremsstrahlung X-rays, which are refracted by a silicon single crystal of (1 1 1) plane. The photon energy width is primarily determined by the distance between the X-ray source and the crystal plate, and the irradiation field increases with increases in the distance between the crystal and the imaging plate. Because we employed the microfocus tube, phase-contrast effect was added in the radiography.

The microfocus generator produced maximum X-ray intensity was approximately 50 μGy/s at 1.0 m from the source, but the intensity was decreased substantially after the diffraction. Therefore, a high-current tungsten tube with a large focus should be employed in cases where the phase-contrast radiography is not employed.

Fig. 7. Radiograms of a vertebra.

The magnification method is needed in phase-contrast radiography, and the method increases the spatial resolution of the digital radiography. Next, in conventional cohesion radiography, the spatial resolution is primarily determined by the sampling pitch of the CR system of 87.5 μm. Therefore, to improve the spatial resolution in cohesion radiography, the resolution of the CR system should be improved to approximately 50 μm (Konica Minolta Regius 190). In addition, the spatial resolution can be improved easily to approximately 50 μm or less in cases where an X-ray film is employed.

In this experiment, although we employed the (1 1 1) plane to perform soft radiography, other planes should be employed to perform high-photon-energy radiography. In conjunction with an analyzer crystal, this

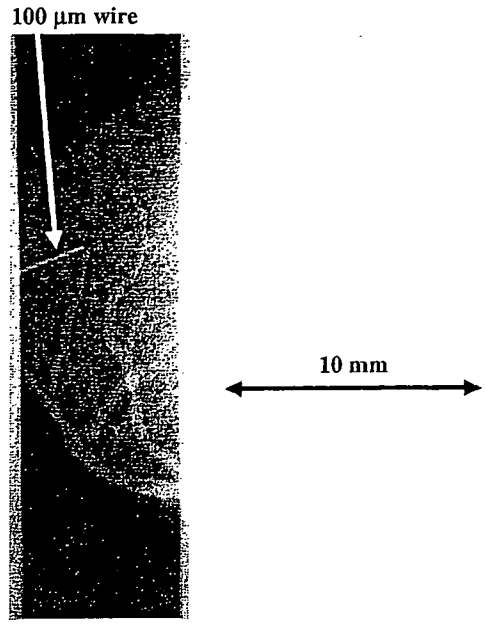

Fig. 8. Angiogram of a rabbit heart.

narrow-photon-energy cone-beam radiography using a microfocus X-ray tube could be useful for phase-contrast radiography as an alternative to radiography using synchrotrons.

Acknowledgments

This work was supported by Grants-in-Aid for Scientific Research (13470154, 13877114, 16591181, and 16591222) and Advanced Medical Scientific Research from MECSST, Health and Labor Sciences Research Grants (RAMT-nano-001, RHGTEFB-genome-005 and RHGTEFB-saisei-003), Grants from the Keiryo Research Foundation, the Promotion and Mutual Aid Corporation for Private Schools of Japan, the Japan Science and Technology Agency (JST), and the New Energy and Industrial Technology Development Organization (NEDO, Industrial Technology Research Grant Program in '03).

References

Ando, M., Maksimenko, M., Sugiyama, H., Pattanasiriwisawa, W., Hyodo, K., Uyama, C., 2002. A simple X-ray dark- and bright- field imaging using achromatic Laue optics. Jpn. J. Appl. Phys. 41, L1016–L1018.

Davis, T.J., Gao, D., Gureyev, T.E., Stevenson, A.W., Wilkins, S.W., 1995. Phase-contrast imagimg of weakly absorbing materials using hard X-rays. Nature 373, 595–597.

Hyodo, K., Ando, M., Oku, Y., Yamamoto, S., Takeda, T., Itai, Y., Ohtsuka, S., Sugishita, Y., Tada, J., 1998. Development of a two-dimensional imaging system for clinical applications of intravenous coronary angiography using intense synchrotron radiation produced by a multipole wiggler. J. Synchrotron Rad. 5, 1123–1126.

Ishisaka, A., Ohara, H., Honda, C., 2000. A new method of analyzing edge effect in phase contrast imaging with incoherent X-rays. Opt. Rev. 7, 566–572.

Momose, A., Takeda, T., Itai, Y., Hirano, K., 1996. Phase-contrast X-ray computed tomography for observing biological soft tissues. Nature Med 2, 473–475.

Mori, H., Hyodo, K., Tanaka, E., Mohammed, M.U., Yamakawa, A., Shinozaki, Y., Nakazawa, H., Tanaka, Y., Sekka, T., Iwata, Y., Honda, S., Umetani, K., Ueki, H., Yokoyama, T., Tanioka, K., Kubota, M., Hosaka, H., Ishizawa, N., Ando, M., 1996. Small-vessel radiography in situ with monochromatic synchrotoron radiation. Radiology 201, 173–177.

Sato, E., Kimura, S., Kawasaki, S., Isobe, H., Takahashi, K., Tamakawa, Y., Yanagisawa, T., 1990. Repetitive flash X-ray generator utilizing a simple diode with a new type of energy-selective function. 2343–2348. Rev. Sci. Instrum. 61, 2343–2348.

Sato, E., Takahashi, K., Sagae, M., Kimura, S., Oizumi, T., Hayasi, Y., Tamakawa, Y., Yanagisawa, T., 1994a. Sub-kilohertz flash X-ray generator utilizing a glass-enclosed cold-cathode triode. Med. Biol. Eng. Comput. 32, 289–294.

Sato, E., Sagae, M., Takahashi, K., Shikoda, A., Oizumi, T., Hayasi, Y., Tamakawa, Y., Yanagisawa, T., 1994b. 10 kHz microsecond pulsed X-ray generator utilizing a hot-cathode triode with variable durations for biomedical radiography. Med. Biol. Eng. Comput. 32, 295–301.

Sato, E., Sato, K., Tamakawa, Y., 2000. Film-less computed radiography system for high-speed imaging. Ann. Rep. Iwate Med. Univ. Sch. Lib. Arts Sci. vol. 35, pp. 13-23.

Sato, E., Hayasi, Y., Germer, R., Tanaka, E., Mori, H., Kawai, T., Obara, H., Ichimaru, T., Takayama, K., Ido, H., 2003a. Irradiation of intense characteristic X-rays from weakly ionized linear molybdenum plasma. Jpn. J. Med. Phys. 23, 123–131.

Sato, E., Hayasi, Y., Germer, R., Tanaka, E., Mori, H., Kawai, T., Ichimaru, T., Takayama, K., Ido, H., 2003b. Quasi-monochromatic flash X-ray generator utilizing weakly ionized linear copper plasma. Rev. Sci. Instrum. 74, 5236–5240.

Sato, E., Sagae, M., Tanaka, E., Hayasi, Y., Germer, R., Mori, H., Kawai, T., Ichimaru, T., Sato, S., Takayama, Y., Ido, H., 2004a. Quasi-monochromatic flash X-ray generator utilizing a disk-cathode molybdenum tube. Jpn. J. Appl. Phys. 43, 7324–7328.

Sato, E., Hayasi, Y., Germer, R., Tanaka, E., Mori, H., Kawai, T., Ichimaru, T., Sato, S., Takayama, K., Ido, H., 2004b. Sharp characteristic X-ray irradiation from weakly ionized linear plasma. J. Electron Spectrosc. Related Phenom. 137-140, 713–720.

Sato, E., Tanaka, E., Mori, H., Kawai, T., Ichimaru, T., Sato, S., Takayama, K., Ido, H., 2004c. Demonstration of enhanced K-edge angiography using a cerium target X-ray generator. Med. Phys. 31, 3017–3021.

Sato, E., Tanaka, E., Mori, H., Kawai, T., Ichimaru, T., Sato, S., Takayama, Y., Ido, H., 2005a. Compact monochromatic flash X-ray generator utilizing a disk-cathode molybdenum tube. Med. Phys. 32, 49–54.

Sato, E., Tanaka, E., Mori, H., Kawai, T., Sato, S., Takayama, Y., 2005b. High-speed enhanced K-edge angiography utilizing cerium plasma X-ray generator. Opt. Eng. 44, 049001–049016.

Sato, E., Tanaka, E., Mori, H., Kawai, T., Sato, S., Takayama, Y., 2005c. Clean monochromatic X-ray irradiation from weakly ionized linear copper plasma. Opt. Eng. 44, 049002–049016.

Shikoda, A., Sato, E., Sagae, M., Oizumi, T., Tamakawa, Y., Yanagisawa, T., 1994. Repetitive flash X-ray generator having a high-durability diode driven by a two-cable-type line pulser. Rev. Sci. Instrum. 65, 850–856.

Takahashi, K., Sato, E., Sagae, M., Oizumi, T., Tamakawa, Y., Yanagisawa, T., 1994. Fundamental study on a long-duration flash X-ray generator with a surface-discharge triode. Jpn. J. Appl. Phys. 33, 4146–4151.

Thompson, A.C., Zeman, H.D., Brown, G.S., Morrison, J., Reiser, P., Padmanabahn, V., Ong, L., Green, S., Giacomini, J., Gordon, H., Rubenstein, E., 1992. First operation of the medical research facility at the NSLS for coronary angiography. Rev. Sci. Instrum. 63, 625–628.

Wilkins, S.W., Gureyev, Gao, T.E., Pogany, D.A., Stevenson, A.W., 1996. Phase-contrast imaging using polychromatic hard X-rays. Nature 384, 335–338.

Available online at www.sciencedirect.com
ScienceDirect
Radiation Physics and Chemistry 75 (2006) 1841–1849
Radiation Physics and Chemistry
www.elsevier.com/locate/radphyschem

K-edge angiography utilizing a tungsten plasma X-ray generator in conjunction with gadolinium-based contrast media

Eiichi Sato[a,*], Yasuomi Hayasi[a], Etsuro Tanaka[b], Hidezo Mori[c], Toshiaki Kawai[d], Takashi Inoue[e], Akira Ogawa[e], Shigehiro Sato[f], Kazuyoshi Takayama[g], Jun Onagawa[h], Hideaki Ido[h]

[a]*Department of Physics, Iwate Medical University, 3-16-1 Honchodori, Morioka 020-0015, Japan*
[b]*Department of Nutritional Science, Faculty of Applied Bio-science, Tokyo University of Agriculture, 1-1-1 Sakuragaoka, Setagaya-ku 156-8502, Japan*
[c]*Department of Cardiac Physiology, National Cardiovascular Center Research Institute, 5-7-1 Fujishirodai, Suita, Osaka 565-8565, Japan*
[d]*Electron Tube Division #2, Hamamatsu Photonics K. K., 314-5 Shimokanzo, Iwata 438-0193, Japan*
[e]*Department of Neurosurgery, School of Medicine, Iwate Medical Universichimaru, Morioka 020-8505, Japan*
[f]*Department of Microbiology, School of Medicine, Iwate Medical University, 19-1 Uchimaru, Morioka 020-8505, Japan*
[g]*Shock Wave Research Center, Institute of Fluid Science, Tohoku University, 2-1-1 Katahira, Sendai 980-8577, Japan*
[h]*Department of Applied Physics and Informatics, Faculty of Engineering, Tohoku Gakuin University, 1-13-1 Chuo, Tagajo 985-8537, Japan*

Accepted 23 November 2005

Abstract

The tungsten plasma flash X-ray generator is useful in order to perform high-speed enhanced K-edge angiography using cone beams because K-series characteristic X-rays from the tungsten target are absorbed effectively by gadolinium-based contrast media. In the flash X-ray generator, a 150 nF condenser is charged up to 80 kV by a power supply, and flash X-rays are produced by the discharging. The X-ray tube is a demountable diode, and the turbomolecular pump evacuates air from the tube with a pressure of approximately 1 mPa. Since the electric circuit of the high-voltage pulse generator employs a cable transmission line, the high-voltage pulse generator produces twice the potential of the condenser charging voltage. At a charging voltage of 80 kV, the estimated maximum tube voltage and current were approximately 160 kV and 40 kA, respectively. When the charging voltage was increased, the characteristic X-ray intensities of tungsten K_α lines increased. The K_α lines were clean, and hardly any bremsstrahlung rays were detected. The X-ray pulse widths were approximately 110 ns, and the time-integrated X-ray intensity had a value of approximately 0.35 mGy at 1.0 m from the X-ray source with a charging voltage of 80 kV. Angiography was performed

*Corresponding author.
E-mail address: dresato@iwate-med.ac.jp (E. Sato).

0969-806X/$ - see front matter
doi:10.1016/j.radphyschem.2005.11.015

using a film-less computed radiography (CR) system and gadolinium-based contrast media. In angiography of non-living animals, we observed fine blood vessels of approximately 100 μm with high contrasts.

PACS: 52.59.Mv; 52.80.Vp; 87.59.Dj; 87.64.Gb

Keywords: Angiography; Gadolinium-based contrast media; Characteristic X-rays; Quasi-monochromatic X-rays; Tungsten K_α lines

1. Introduction

The successful uses of monochromatic parallel beams from synchrotron orbital radiation in recent years have greatly increased the demand for phase-contrast radiography (Davis et al., 1995; Momose et al., 1996; Ando et al., 2002) and enhanced K-edge angiography (Thompson et al., 1992; Mori et al., 1996; Hyodo et al., 1998). In particular, the parallel beams with photon energies of approximately 35 keV have been employed to perform angiography, because the beams are absorbed effectively by iodine-based contrast media with a K-absorption edge of 33.2 keV. Without using a synchrotron, we have developed an X-ray generator utilizing a cerium-target tube, and have performed cone-beam K-edge angiography achieved with cerium K_α rays of 34.6 keV (Sato et al., 2004a, b, c).

Gadolinium-based contrast media with a K-edge of 50.2 keV have been employed to perform magnetic resonance angiography (MRA), and the gadolinium density has been increasing. In view of this situation, ytterbium K_α rays (52.0 keV) are useful for enhanced K-edge angiography, because the K_α rays are absorbed effectively by gadolinium media. As compared with angiography using iodine media, the absorbed dose can be decreased considerably utilizing angiography achieved with gadolinium media. However, because ytterbium is a lanthanide series element and tends to oxidize in the atmosphere, K_α rays of tantalum (57.1 keV) and tungsten (58.9 keV) are also useful to perform angiography.

To produce high-dose-rate X-rays, several different flash X-ray generators have been developed (Sato et al., 1990, 1994a, b; Shikoda et al., 1994; Takahashi et al., 1994), and plasma flash X-ray generators (Sato et al., 2003a, b, 2004a, b, c, 2005a, b, c) have been developed to perform a preliminary experiment for producing hard X-ray lasers. In the plasma, the bremsstrahlung X-rays are absorbed effectively and are converted into fluorescent rays, and intense and clean K-series characteristic X-rays of nickel and copper have been produced from the axial direction of weakly ionized linear plasma. However, it is difficult to increase the photon energies of characteristic X-rays because the plasma transmits high-photon-energy bremsstrahlung X-rays. In view of this situation, we have developed a compact flash X-ray generator (Sato et al., 2004a, b, c, 2005a, b, c) and have succeeded in producing clean high-photon-energy characteristic X-rays utilizing the angle dependence of bremsstrahlung X-rays, because bremsstrahlung rays are not emitted in the opposite direction to that of electron trajectory in Sommerfeld's theory.

In this article, we describe an intense quasi-monochromatic plasma flash X-ray generator with a tungsten target tube, and used it to perform a preliminary study on angiography achieved with tungsten K_α rays.

2. Principle of K-edge angiography

Fig. 1 shows the mass attenuation coefficients of gadolinium at the selected energies; the coefficient curve is discontinuous at the gadolinium K-edge. The average photon energy of the tungsten K_α lines is shown above the gadolinium K-edge. The average photon energy is 58.9 keV, and gadolinium contrast media with a K-absorption edge of 50.2 keV absorb the lines easily. Therefore, blood vessels were observed with high contrasts.

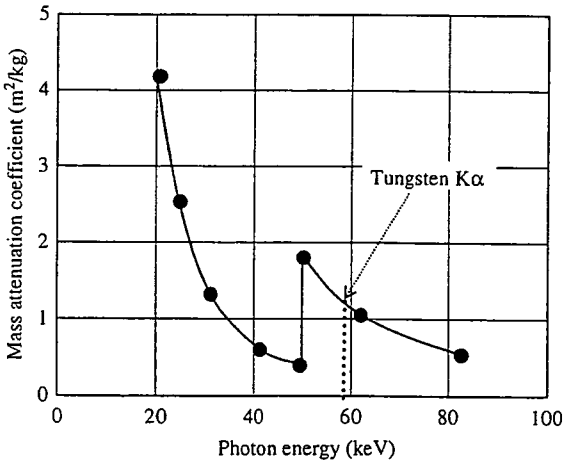

Fig. 1. Mass attenuation coefficients of gadolinium. The average photon energy of tungsten K_α lines is shown above gadolinium K edge.

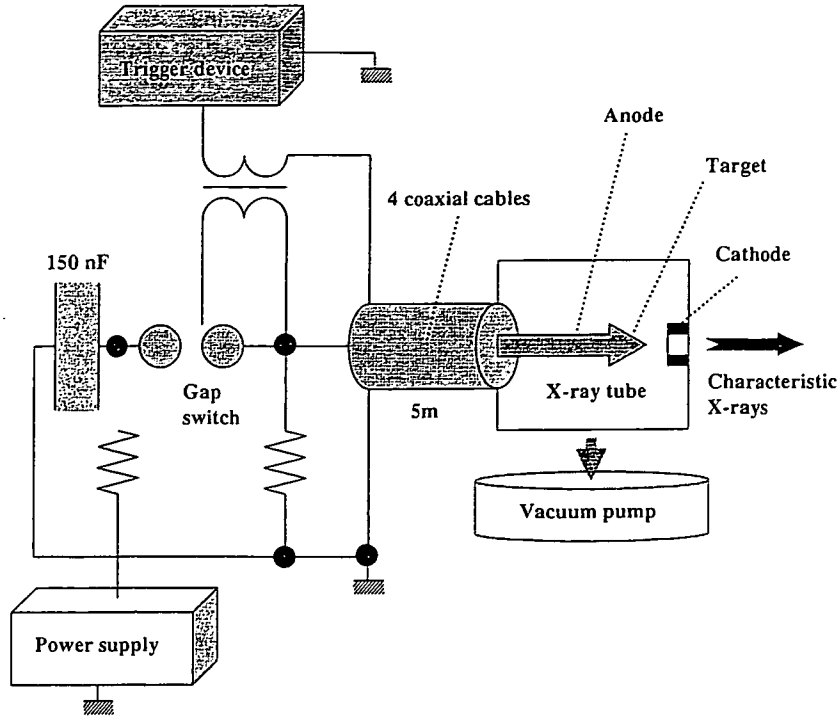

Fig. 2. Block diagram including the high-voltage circuit of the intense quasi-monochromatic plasma flash X-ray generator with a tungsten-target tube.

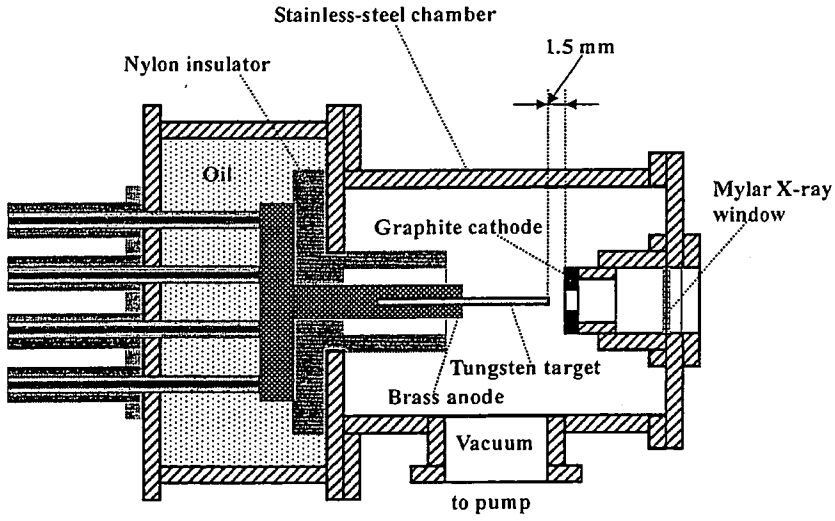

Fig. 3. Schematic drawing of a flash X-ray tube with a rod-shaped tungsten target.

3. Generator

3.1. High-voltage circuit

Fig. 2 shows a block diagram of a high-intensity plasma flash X-ray generator. The generator consists of the following essential components: a high-voltage power supply, a high-voltage condenser with a capacity of approximately 150 nF, an air gap switch, a turbomolecular pump, a thyratron pulse generator as a trigger device and a flash X-ray tube. In this generator, a coaxial cable transmission line is employed in order to

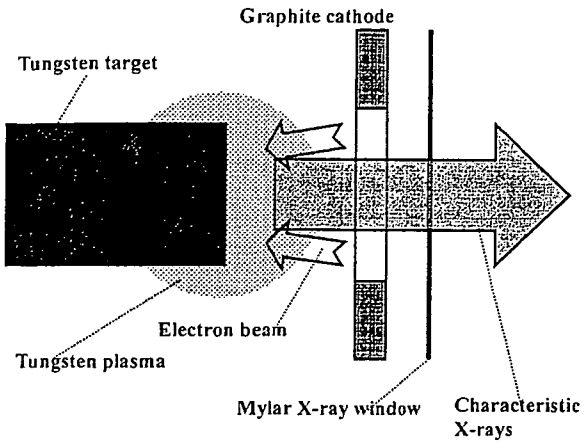

Fig. 4. Irradiation of K-series characteristic X-rays of tungsten.

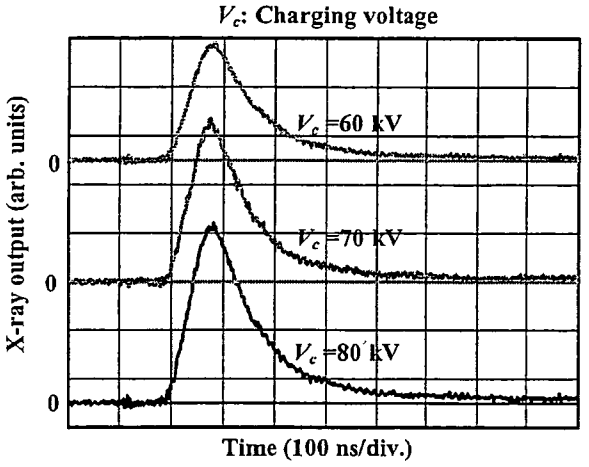

Fig. 5. X-ray outputs detected using a combination of a plastic scintillator and a photomultiplier.

increase maximum tube voltage using high-voltage reflection. The high-voltage main condenser is charged up to 80 kV by the power supply, and electric charges in the condenser are discharged to the tube through the four cables after closing the gap switch with the trigger device.

3.2. X-ray tube

The X-ray tube is a demountable cold-cathode diode that is connected to the turbomolecular pump with a pressure of approximately 1 mPa (Fig. 3). This tube consists of the following major parts: a ring-shaped graphite cathode with an inside diameter of 4.5 mm, a stainless-steel vacuum chamber, a nylon insulator, a polyethylene terephthalate (Mylar) X-ray window 0.25 mm in thickness and a rod-shaped tungsten target 3.0 mm in diameter. The distance between the target and cathode electrodes can be regulated from the outside of the tube, and is set to 1.5 mm. As electron beams from the cathode electrode are roughly converged to the target by the electric field in the tube, evaporation leads to the formation of weakly ionized plasma, consisting of tungsten ions and electrons, around the target. Because bremsstrahlung rays are not emitted in the opposite direction to that of electron trajectory (Fig. 4), tungsten K-series characteristic X-rays can be produced without using a filter.

4. Characteristics

4.1. Tube voltage and current

In this generator, it was difficult to measure the tube voltage and current since the tube voltages were high, and there was no space to set a current transformer for measuring the tube current. Currently, the voltage and

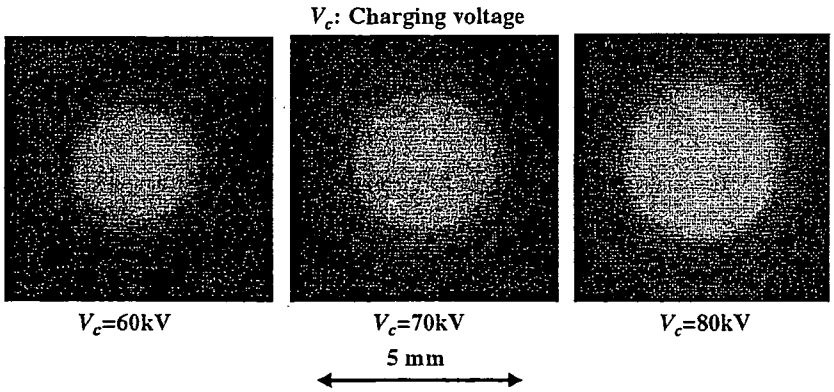

Fig. 6. Images of characteristic X-ray source obtained using a pinhole camera with changes in the charging voltage.

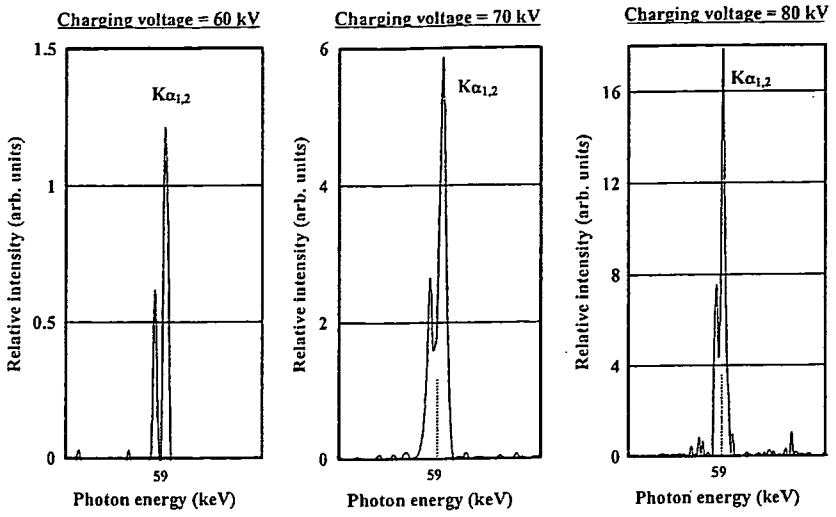

Fig. 7. X-ray spectra from a tungsten target. The spectra were measured using a transmission type spectrometer with a lithium fluoride curved crystal.

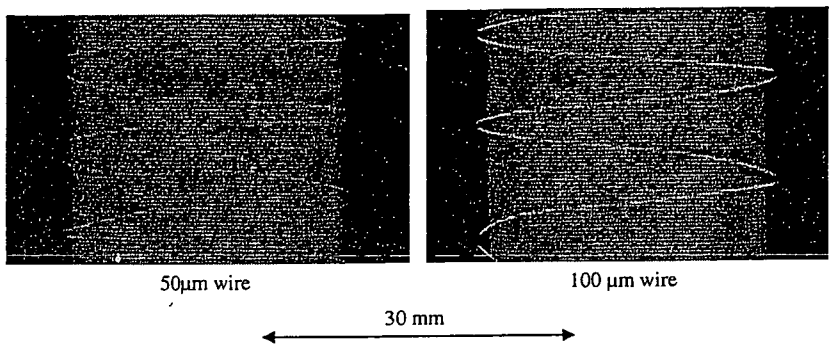

Fig. 8. Radiograms of tungsten wires coiled around rods made of polymethyl methacrylate.

current roughly display damped oscillations. When the charging voltage was increased, both the maximum tube voltage and current increased. At a charging voltage of 80 kV, the estimated maximum values of the tube voltage and current were approximately 160 kV (two times the charging voltage) and 40 kA, respectively.

4.2. X-ray output

X-ray output pulse was detected using a combination of a plastic scintillator and a photomultiplier (Fig. 5). The X-ray pulse height substantially increased with corresponding increases in the charging voltage. The X-ray pulse widths were approximately 110 ns, and the time-integrated X-ray intensity measured by a thermoluminescence dosimeter (Kyokko TLD Reader 1500 having MSO-S elements without energy compensation) had a value of approximately 0.35 mGy at 1.0 m from the X-ray source with a charging voltage of 80 kV.

4.3. X-ray source

In order to observe the plasma X-ray source, we employed a 100-μm-diameter pinhole camera and an X-ray film (Polaroid XR-7) (Fig. 6). When the charging voltage was increased, the plasma X-ray source grew, and both spot dimension and intensity increased. Because the X-ray intensity is the highest at the center of the spot, both the dimension and intensity decreased according to both increases in the thickness of a filter for absorbing X-rays and decreases in the pinhole diameter.

4.4. X-ray spectra

X-ray spectra were measured using a transmission-type spectrometer with a lithium fluoride curved crystal 0.5 mm in thickness. The X-ray intensities of the spectra were detected by an imaging plate of a computed radiography (CR) system (Sato et al., 2000) (Konica Minolta Regius 150) with a wide dynamic range, and

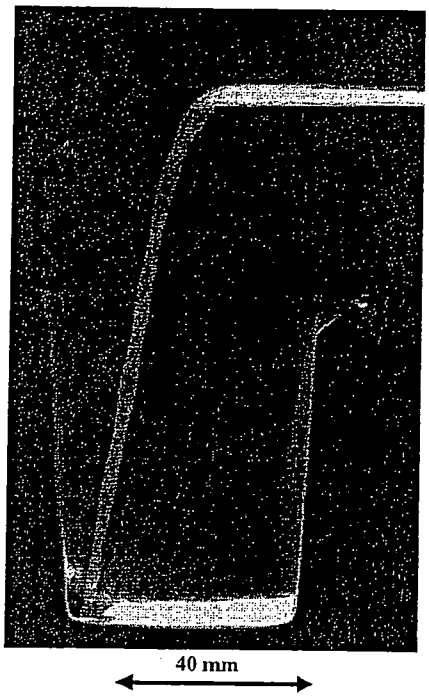

Fig. 9. Radiogram of water falling into polypropylene beaker from a glass test tube.

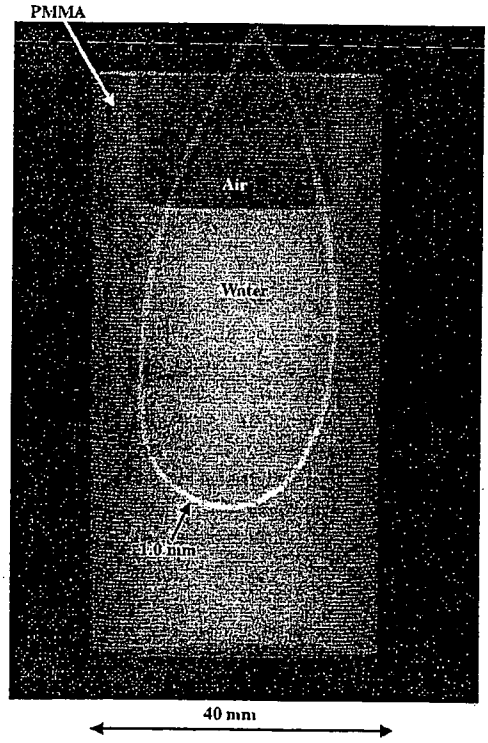

Fig. 10. Angiography of a Teflon tube using a contrast medium which contains approximately 65% gadodiamidehydrate.

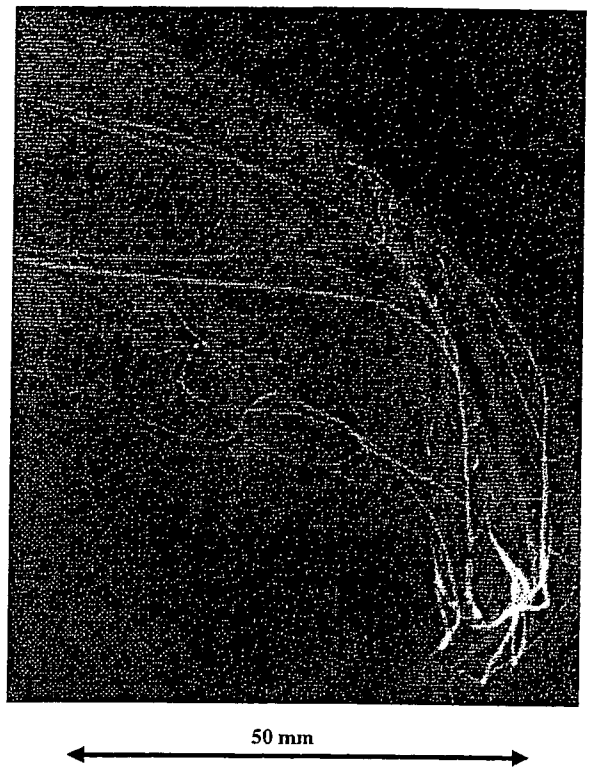

Fig. 11. Angiography of a rabbit ear using gadolinium oxide powder.

relative X-ray intensity was calculated from Dicom original digital data corresponding to X-ray intensity; the data was scanned by Dicom viewer in the film-less CR system. Subsequently, the relative X-ray intensity as a function of the data was calibrated using a conventional X-ray generator, and we confirmed that the intensity was proportional to the exposure time. Fig. 7 shows measured spectra from the tungsten target. We observed clean K_α lines, while bremsstrahlung rays were hardly detected. The K_α intensity substantially increased with increases in the charging voltage.

5. Angiography

The flash angiography was performed by the CR system at 1.2 m from the X-ray source, and the charging voltage was 80 kV.

Firstly, rough measurements of spatial resolution were made using wires. Fig. 8 shows radiograms of tungsten wires coiled around rods made of polymethyl methacrylate (PMMA). Although the image contrast decreased somewhat with decreases in the wire diameter, due to blurring of the image caused by the sampling pitch of 87.5 μm, a 50-μm-diameter wire could be observed.